Wavelet-Based Representation of Biological Shapes

Bin Dong[1], Yu Mao[2], Ivo D. Dinov[3], Zhuowen Tu[3], Yonggang Shi[3], Yalin Wang[3], and Arthur W. Toga[3]

[1] Department of Mathematics, University of California, San Diego, 9500 Gilman Drive, La Jolla, CA, 92093-0112
[2] Department of Mathematics, University of California, Los Angeles, CA, 90095-1555
[3] Center for Computational Biology, Laboratory of Neuro Imaging, 635 S. Charles Young Dr., #225, University of California, Los Angeles, Los Angeles, CA, USA, 90055

Abstract. Modeling, characterization and analysis of biological shapes and forms are important in many computational biology studies. Shape representation challenges span the spectrum from small scales (e.g., microarray imaging and protein structure) to the macro scale (e.g., neuroimaging of human brains). In this paper, we present a new approach to represent and analyze biological shapes using wavelets. We apply the new technique to multi-spectral shape decomposition and study shape variability between populations using brain cortical and subcortical surfaces. The wavelet-space-induced shape representation allows us to study the multi-spectral nature of the shape's geometry, topology and features. Our results are very promising and, comparing to the spherical-wavelets method, our approach is more compact and allows utilization of diverse wavelet bases.

1 Literature Reviews

Imaging, representation, geometric modelling and topological characterization of shape and form are important components of Computational Biology. They apply across the vast length scales between genotypes to phenotypes, from the small scale of microarray imaging for genomic, to the larger scale of neuroimaging of human brains. Here we review the existing techniques and algorithms and present a new approach for representation and analysis of biological shapes using wavelets. We apply the new method to multi-spectral shape decomposition and study shape variability between populations using brain cortical and subcortical surfaces.

Recently, N. Hacker et al. used conformal mapping and spherical wavelets to analyze biological shapes (see [1–3]). Their idea is first mapping the original shape onto a unit 2-sphere using a certain conformal mapping so that one obtains a $\mathbb{R}^3$-valued function f defined on the sphere; and then interpolate the function onto the regular triangular mesh on the sphere (which is generated by recursively subdividing an icosahedron); and then finally, apply spherical wavelet transform to the interpolated function. The spherical wavelets they used were introduced

by P. Schröder and W. Sweldens in [4], which were constructed using lifting scheme (see W. Sweldens [5] and F. Arandiga et. al. [6]).

In this section, we also start from a $\mathbb{R}^3$-valued function f determined by a certain mapping from $\mathbb{R}^3$ to S^2. After that, we linearly interpolate the function onto a triangular mesh, which is generated by recursively subdividing an octahedron in $\mathbb{R}^3$ (not restricted on the sphere) and then transforming the mesh onto the sphere. This method was first introduced by E. Praun and H. Hoppe (see [7]) in the context of computer graphics. The major advantage of it is that we can transform the subdivided octahedron to a unit square so that we obtain an image with $\mathbb{R}^3$-valued entries (which were called geometric image in [7]), and then we can apply traditional X-lets (e.g. wavelets, framelets, curvelets etc.) decomposition. In this way we have plenty of good bases and frames (redundant systems) to choose according the application we have.

Understanding the relationship between the structure and function of the human brain in vivo has been the driving motivation for many neurosciences research for centuries. The research efforts not only focus on studying normal development but also understanding alterations in various clinical populations including schizophrenia, Huntington's disease, Alzheimer's disease, Williams Syndrome, autism, stroke, chronic drug abuse, as well as pharmacological interventions. For instance, there are multiple studies underway to quantify the differences between the brain structure of schizophrenic patients and healthy individuals in different stages of this disease. Detection of these significant differences via neuroimaging studies is not only useful to elucidate the link between change in cognitive profile and change in brain structure, but also to improve diagnosis particularly in early stages of the disease. With the increasing interest in carrying out such studies with large numbers of subjects, there is a need for a unified framework for image segmentation to identify the structure of interest (e.g. caudate, ventricles, cerebral cortex, sulcal regions) (see Z. Tu et. al. [8]), and morphometric analysis which requires methods for shape representation, shape comparison, and change in shape measurement (see P. Thompson and A. Toga [9]).

2 Method

In this section we describe our test data and the specific approach we took to represent shape using wavelets, as well as the statistical analysis we carry on the wavelet-based shape decomposition to identify group, population, time or variation differences. Throughout this paper, all shapes are assumed to be close surfaces in $\mathbb{R}^3$ with genus zero.

2.1 Data

Cortical Models: Surface objects of normal subjects and Williams syndrome patients were used to explore the power of our method to synthesize the energy of the shape content in a few wavelet coefficients. The demographics of the

population included age (29.2 9.0), genders (approximately 50/50) and IQ scores, P. Thompson et. al. [10]. Non-brain tissue (i.e., scalp, orbits) was removed from the images, and each image volume was re-sliced into a standard orientation who "tagged" 20 standardized anatomical landmarks in each subject's image data set that corresponded to the same 20 anatomical landmarks defined on the ICBM53 average brain (see Mazziotta et al. [11], Thompson et. al. [12]). Automated tissue segmentation was conducted for each volume data set to classify voxels as most representative of gray matter, white matter, CSF, or a background class (representing extra cerebral voxels in the image) on the basis of signal intensity. The procedure fits a mixture of Gaussian distributions to the intensities in each image before assigning each voxel to the class with the highest probability, Shattuck et. al. [13]. Then each individual's cortical surface was extracted and three-dimensionally rendered using automated software, MacDonald [14]. Each resulting cortical surface was represented as a high-resolution mesh of 131,072 surface triangles spanning 65,536 surface points.

Hippocampal surfaces: High-resolution MRI scans were acquired from 12 AD patients ages 68.4 1.9 and 14 matched controls 71.4 0.9, each scanned twice, 2.1 0.4 years apart. 3D parametric mesh models of the left and right hippocampi and temporal horns were manually, Thompson et. al. [15]. For each scan, a radio frequency bias field correction algorithm eliminated intensity drifts due to scanner field inhomogeneity, using a histogram spline sharpening method, Sled et. al. [16]. Images were then normalized by transforming them to ICBM53 stereotaxic space, Evens et. al. [17], with automated image registration software, Collins et. al. [18]. To equalize image intensities across subjects, registered scans were histogram-equalized.

Each 3D surface is mapped to a unit sphere in $\mathbb{R}^3$ with 1-to-1 correspondence. For cortical surfaces, the conformal mapping method of Shi et. al. [19, 20], is used for hippocampal surfaces and that of Gu et. al. [21] for cortical surfaces. For hippocampal surfaces, harmonic maps to the sphere are computed under the constraints of a set of automatically detected landmark curves (see [19, 20]). Figures (a) and (b) in Figure 1 shows a hippocampal shape and the mapping of it on a unit sphere respectively, where in the latter, (x, y, z) values on each vertex of the sphere are color-coded by RGB.

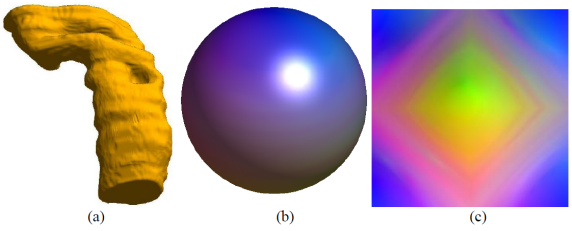

Fig. 1. Figure (a) is the given shape; (b) is the spherical function obtained by surface mapping; (c) is the geometric image.

2.2 Wavelet-Based Representation for Shapes

From the previous section, we got a function f defined on the unit sphere S^2, which has vector values in $\mathbb{R}^3$. However, the values of the function were only given on an irregular grid on the sphere. To apply the wavelet transform, we need to get the value of the function on a much more regular spherical grid. There are many approaches to get such kind of grids. The construction of the spherical mesh grid, sometimes called spherical triangular map, is an interesting subject itself (see e.g. Buss and Fillmore [22], and Praun and Hoppe [7]). The basic idea is to start from a polyhedral base, which gives a simple but perfect grid on sphere, and then use some appropriate scheme to subdivide the mesh. A comparison of such techniques can be found in [7].

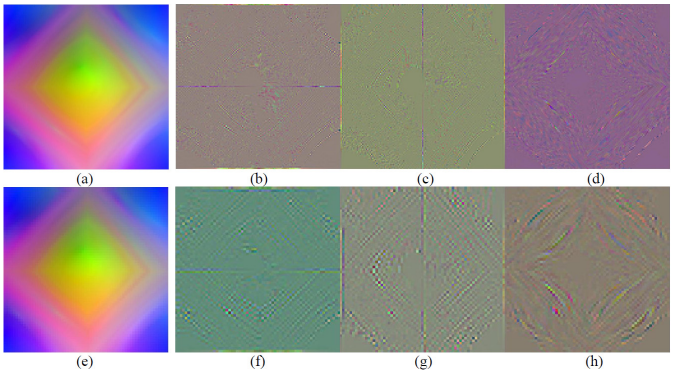

Fig. 2. Two-levels wavelet decomposition: (a) and (e) are the low frequency coefficients of level one and two; (b)-(d) are wavelet coefficients of level 1 and band 1-3; (f)-(h) are wavelet coefficients of level 2 and band 1-3.

In our approach, we start from a recursive subdivision of the octahedral base. By mapping the subdivision grid onto the unit sphere, we get a regular grid structure on the sphere, and the function values on such a spherical grid can be obtained by linear interpolation. The reason we choose octahedron is that it can be unfolded to a plain image easily. Therefore, we can build a 1-1 map between a sphere and an image without too much distortion, and the data of a shape is transformed to a $\mathbb{R}^3$-valued function defined on a plain image, which gives a geometric image (as shown in (c) Figure 1). Since the mesh on the plain image is nothing but a Cartesian grid, a huge family of X-lets can be used to analyze properties of the geometric image. The wavelets that we shall use in the following experiments are Daubechies' Biorthogonal Wavelets [23]. We note that the boundary condition is a little complicated in this case. Topological saying, the two halves of each side of the image must be identified with each other (see [7] for more details). Thus, we need to setup corresponding boundary rules for the wavelet filters.

We now summarize the entire multiscale representation process in the following Algorithm 1. Figure 2 shows how the decomposition is carried out to the geometric image we have. Since all low frequency and wavelet coefficients has x, y, and z three components, all coefficients are visualized as color images.

Algorithm 1 Wavelet-Based Representation for Shapes

Given some triangulated biological shape (V, T), where $V \in \mathbb{R}^3$ is the vertex set and T is triangulation.
1. Find the mapping $\mathcal{M} : V \mapsto S^2$, which also induces a triangulation on S^2 denoted as $(V_S, T_S) =: M_S$. Define $f_0 = \mathcal{M}^{-1} : S^2 \mapsto V$ (Figure 1(b)).
2. Recursively subdivide an octahedron uniformly in $\mathbb{R}^3$ up to certain level N. Then project the mesh on to S^2 and obtain a mesh on S^2 denoted as $(V_N, T_N) =: M_N$.
3. Interpolate f_0 from M_S to M_N and obtain a new spherical function f, which, by construction, can be easily transformed to a geometric image (Figure 1(c)).
4. Perform regular X-let decomposition and reconstruction (with proper boundary conditions).

2.3 Multiscale Curvature-Like Characterization

As shown in Figure 2 above, for each level and band of the wavelet coefficients, we have x, y, and z three components. The coefficient vectors reflect details of the shape at each position and scale. Indeed, the wavelet vectors can be treated as the displacement between the observed position and the predicted position calculated from the convolution of the wavelet filter and the scale coefficients of the neighboring vertices. Therefore, the direction of the wavelet vector gives us some information of the local geometric properties. For example, if we consider the wavelet vector at a local sunken area, then the approximated position interpolated from the neighboring vertices should be outer than the observed vertex, which means that the wavelet vector is pointing outwards.

However, we cannot tell the geometric property of the shape from the wavelet coefficients directly, and a single wavelet coefficient itself is geometrically meaningless, so we combine the three components by calculating the inner product of the wavelet vector and the normal vector of the shape. As what we explained above, these inner products reflect geometric property at the corresponding position. In this way, a so called multiscale curvature-like characterization of the shape is obtained: For given scale (or level), we compute normal of the shape at all positions under that scale and take the inner product of the normal with the wavelet coefficient vector. We then obtain a set of curvature-like coefficients within each level and band. The statistical analysis given in the following section is based on this representation. Figure 3 shows how this representation can be used to find cortical sulci and gyri.

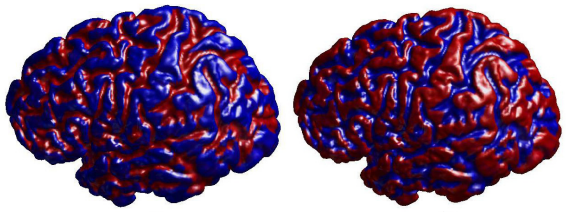

Fig. 3. Red regions in figure (a) and (b) are the sulcal and gyral regions respectively.

3 Numerical Experiments

3.1 Sparsity of the Representation

One of the most important properties of traditional wavelet transform is that it gives a MSR of the underlying function and the representation is sparse. We now show that our method as discussed in the previous section also gives a sparse MSR for the biological shapes we have. Figure 4 and 5 shows the MSR provided by the wavelet transform, and Figure 6 and 7 shows the sparsity of the representation, where one can see that even with only 2500 coefficients, the reconstructed shapes preserve most of the features of the original shapes.

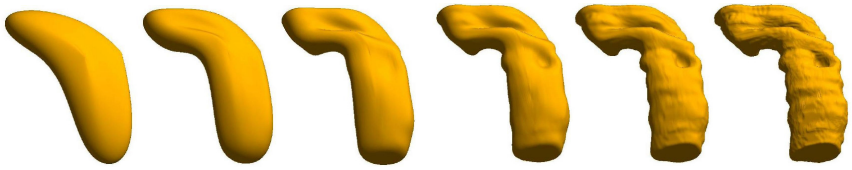

Fig. 4. Figures left to right present a MSR of the hippocampus from courser approximation to finer approximation. The last figure is the original hippocampus.

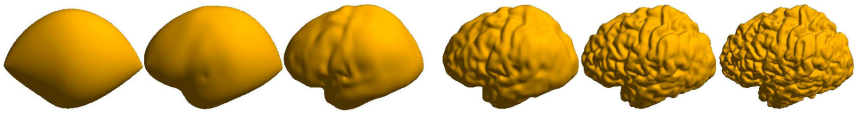

Fig. 5. Figures from left to right present a MSR of the cortex from courser approximation to finer approximation. The last figure is the original cortex.

One advantage of our method over spherical wavelet transform in analyzing biological shapes is that we have a much more flexible choice of wavelets. In

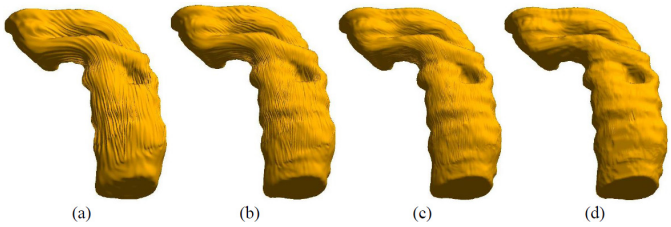

Fig. 6. Figures (a)-(c) are the reconstructed hippocampus using 1000, 2500 and 5000 coefficients, and the relative errors of them from the original shape are 1.171871e-004, 6.172233e-005 and 3.915038e-005 respectively. Figure (d) is the original hippocampus.

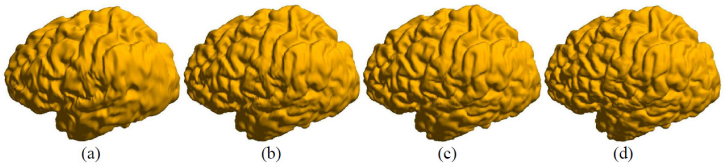

Fig. 7. Figures (a)-(c) are the reconstructed cortices using 1000, 2500 and 5000 coefficients, and the relative errors of them from the original shape are 6.449351e-004, 3.154665e-004 and 1.664914e-004 respectively. Figure (d) is the original cortex.

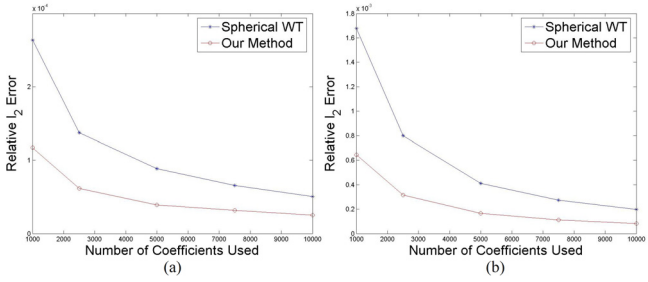

Fig. 8. Figures (a) and (b) are the decay of relative ℓ_2 error verse number of coefficients used, where the underline shapes are the hippocampus and cortex as shown in Figure 6 and 7.

particular, we can choose one wavelet with very high vanishing moments so that the representation is very sparse. Figure 8 below shows a comparison of our method to spherical wavelets as used in [1–3].

The multiscale sparse representation provided by the wavelet transform has many applications. For example, one can do shape compression, or in other words, feature dimension reduction for shapes. One can also do shape denoising via thresholding or shrinkage of wavelet coefficients. Since these kinds of applications are not of our main interest, we shall not explore them in further details.

3.2 Non-Parametric Tests

For given two groups of hippocampus, one from healthy population, the other from the one with Alzheimer's disease, we apply Wilcoxon's rank sum test (see e.g. [24]) to the multiscale curvature-like representation of shapes to find regions on the shape where the two groups are different. The -value we choose in the results below is 0.05. We note that the tests are more reliable in higher levels than those in lower levels. This is because the shape corresponding to a higher level is a smoothed version of the original shape, which means we have more statistical inference of the object. As one can see from below that the higher the level is, the larger each area of significance will be. In Figure 9 below, we used the mean hippocampus as the reference shape, which is calculated by simply taking an average of all the vector values of hippocampus at every position.

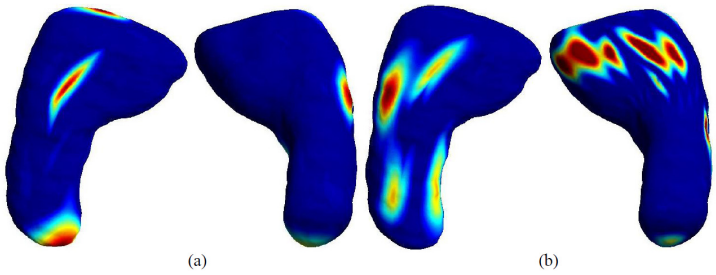

Fig. 9. Figures (a) and (b) show regions of significance of level 5 and 4 respectively. Here, each pair of hippocampus is viewed from the bottom.

4 Discussion

The wavelet-based shape representation technique proposed here allows one to study the geometry, topology and features of general biological shapes using any of the standard wavelet-bases on real-valued Euclidean spaces. The results

we obtained are robust and consistent across individuals and populations. In addition to direct representation and shape characterization, this technique allows us to compute mean shapes and improve the shape-analysis statistical power by concentrating the energy of the shapecharacteristics in few significant wavelet coefficients, Dinov et. al. [5]. We are in the process of validating the new methodology using larger number of subjects, different types of applications (e.g., studying the population-specific differences in the proportion of gyri to sulcal area) and quantitative comparison with spherical-harmonics, spherical wavelets and tensor-based morphometry techniques.

The computational complexity of the algorithm is $O(N \log N)$ relative to the volume size N. We have a Matlab implementation that we are in the process of converting to stand-alone C++ code. We tested the actual computation time of the wavelet decomposition and reconstruction on a PC with Inter(R) Core(TM) 2, 2.13 GHz and 1G physical memory. For a given shape with 65,536 surface points, the computation time is 2-20 seconds, depending on the choice of basis and level of decomposition.

Acknowledgement

This work is funded by the National Institutes of Health through the NIH Roadmap for Medical Research, Grant U54 RR021813. Information on the National Centers for Biomedical Computing can be obtained from

`http://nihroadmap.nih.gov/bioinformatics.`

References

1. Nain, D., Haker, S., Bobick, A., Tannenbaum, A.: Multiscale 3d shape analysis using spherical wavelets. Lecture Notes in Computer Science **3750** (2005) 459
2. Nain, D., Haker, S., Bobick, A., Tannenbaum, A.: Shape-driven 3D segmentation using spherical wavelets. Lecture Notes in Computer Science **4190** (2006) 66
3. Nain, D., Haker, S., Bobick, A., Tannenbaum, A.: Multiscale 3-d shape representation and segmentation using spherical wavelets. IEEE Transactions on Medical Imaging **26** (2007) 598
4. Schröder, P., Sweldens, W.: Spherical wavelets: Efficiently representing functions on the sphere. (1995) 161–172
5. Sweldens, W.: The lifting scheme: A construction of second generation wavelets. SIAM Journal on Mathematical Analysis **29** (1998) 511
6. Aràndiga, F., Donat, R., Harten, A.: Multiresolution based on weighted averages of the hat function I: Linear reconstruction techniques. SIAM Journal on Numerical Analysis **36** (1999) 160–203
7. Praun, E., Hoppe, H.: Spherical parametrization and remeshing. ACM Transactions on Graphics **22** (2003) 340
8. Tu, Z., Zheng, S., Yuille, A., Reiss, A., Dutton, R., Lee, A., Galaburda, A., Dinov, I., Thompson, P., Toga, A.: Automated extraction of the cortical sulci based on a supervised learning approach. IEEE Transactions on Medical Imaging **26** (2007) 541

9. Thompson, P., Toga, A.: A framework for computational anatomy. Computing and Visualization in Science **5** (2002) 13–34
10. Thompson, P., Lee, A., Dutton, R., Geaga, J., Hayashi, K., Eckert, M., Bellugi, U., Galaburda, A., Korenberg, J., Mills, D., et al.: Abnormal cortical complexity and thickness profiles mapped in Williams syndrome. Journal of Neuroscience **25** (2005) 4146–4158
11. Mazziotta, J., Toga, A., Evans, A., Fox, P., Lancaster, J., Zilles, K., Woods, R., Paus, T., Simpson, G., Pike, B., et al.: A probabilistic atlas and reference system for the human brain: International Consortium for Brain Mapping (ICBM). Philosophical Transactions of the Royal Society of London. Series B **356** (2001) 1293
12. Thompson, P., Hayashi, K., De Zubicaray, G., Janke, A., Rose, S., Semple, J., Herman, D., Hong, M., Dittmer, S., Doddrell, D., et al.: Dynamics of gray matter loss in Alzheimer's disease. Journal of Neuroscience **23** (2003) 994
13. Shattuck, D., Sandor-Leahy, S., Schaper, K., Rottenberg, D., Leahy, R.: Magnetic resonance image tissue classification using a partial volume model. NeuroImage **13** (2001) 856–876
14. MacDonald, J.: A method for identifying geometrically simple surfaces from three-dimensional images. PhD Thesis (1998)
15. Thompson, P., Hayashi, K., de Zubicaray, G., Janke, A., Rose, S., Semple, J., Hong, M., Herman, D., Gravano, D., Doddrell, D., et al.: Mapping hippocampal and ventricular change in Alzheimer disease. Neuroimage **22** (2004) 1754–1766
16. Sled, J., Zijdenbos, A., Evans, A.: A nonparametric method for automatic correction of intensity nonuniformity in MRI data. IEEE Transactions on Medical Imaging **17** (1998) 87–97
17. Evans, A., Collins, D., Neelin, P., MacDonald, D., Kamber, M., Marrett, T.: Three-dimensional correlative imaging: applications in human brain mapping. Functional Neuroimaging: Technical Foundations, Thatcher RW, Hallett M, Zeffiro T, John ER, Huerta M [eds.] (1994) 145–162
18. Collins, D., Neelin, P., Peters, T., Evans, A.: Automatic 3D intersubject registration of MR volumetric data in standardized Talairach space. Journal of computer assisted tomography **18** (1994) 192
19. Shi, Y., Thompson, P., de Zubicaray, G., Rose, S., Tu, Z., Dinov, I., Toga, A.: Direct mapping of hippocampal surfaces with intrinsic shape context. Neuroimage **37** (2007) 792–807
20. Shi, Y., Thompson, P., Dinov, I., Osher, S., Toga, A.: Direct cortical mapping via solving partial differential equations on implicit surfaces. Medical image analysis **11** (2007) 207–223
21. Gu, X., Wang, Y., Chan, T., Thompson, P., Yau, S.: Genus zero surface conformal mapping and its application to brain surface mapping. IEEE Transactions on Medical Imaging **23** (2004) 949–958
22. Buss, S., Fillmore, J.: Spherical averages and applications to spherical splines and interpolation. ACM Transactions on Graphics (TOG) **20** (2001) 95–126
23. Daubechies, I.: Ten lectures on wavelets. **CBMS-NSF Lecture Notes, SIAM, nr. 61** (1992)
24. Gibbons, J., Chakraborti, S.: Nonparametric statistical inference. (2003)